https://doi.org/10.1038/s44455-026-00021-0

Penetration and macroscale "hardness" of fully dense FCC granular crystals: experiments and models

Check for updates

Ashta Navdeep Karuriya & Francois Barthelat ✉

The sharp penetration of granular materials is relevant to a variety of applications, including the locomotion of animals and robots on sandy grounds, defensive structures or civil constructions. In traditional granular materials, the grains "flow" around the advancing penetrator like a viscous liquid, which involves frictional dissipation but produces limited resistance to penetration. In this report, we explore the mechanical performance and mechanics of fully dense FCC granular crystals subjected to sharp penetration. These "granular metamaterials", at the boundary between traditional granular materials and architected materials, are about 1000 times more resistant to penetration than traditional granular materials made of randomly distributed spheres. Using experiments and discrete element models, we show that despite the high mechanical confinement of the crystals, frictional sliding along specific slip planes is a prominent deformation mechanism up to the failure of the uppermost layer of grains. In addition, as the indenter is "wedged" between the grains, large compressive forces develop in the transverse directions, which eventually lead to the sudden buckling of the uppermost layer of grains, and to "explosive" failures involving the ejection of grains. As penetration proceeds, this loading-buckling cycle repeats, as layers are defeated in sequence. We finally show that once the surface layers of the crystal are destroyed by the penetrator, the crystal can be "healed" with vibrations and then punctured again with no loss of mechanical performance. These granular "metamaterials" can serve as a platform to develop additional strengthening strategies inspired by metallurgy, and they can find applications for rapid and versatile construction of static structures or as lightweight protective materials in a multitude of applications (e.g., buildings, body armor and vehicles).

Traditional granular materials are large collections of discrete, non-cohesive macroscopic particles generally interacting through frictional contact with complex, non-linear mechanical response: jamming, shear-induced dilatations, cluster formations and shear bands[1,2]. Despite the richness of these mechanisms, the mechanical performance of granular materials is limited because of their poor packing and suboptimal load transfer: The forces between individual grains are localized to small contact areas, and load transfer in granular matter only occurs along thin "force lines" while most of the grains remain free of stress[3]. The resistance of granular materials to penetration has received considerable attention[4–9] because of its relevance to locomotion of animals and robots on sandy grounds, the formation of craters, defensive structures[10] or civil constructions. At quasi-static rates, grain shear bands and other deformation patterns form near the indenter[6,11]. Semi-empirical macroscopic force laws were also proposed to capture depth-dependent Coulomb friction[12,13]. In this model, the grains are assumed to "flow" around the indenter like a viscous liquid[14], with recent studies going so far as using Archimedes' law[15]. As in homogeneous mechanical loading, the resistance of traditional granular material to sharp penetration is limited by the round shape of the grains and by the randomness of their packing. Several strategies were recently proposed to increase the mechanical performance of granular materials. For example, convex polyhedral grains (cubes, tetrahedra and octahedra) promote jamming, thereby increasing the shear strength by 40 to 80% compared to materials based on spheres[16]. Further, there are polyhedral geometries that can be crystallized into fully dense granular crystals, with strength up to sixty times higher than randomly distributed grains. These "granular metamaterials" display complex mechanical response, including nonlinear deformations, crystal plasticity reminiscent of atomistic mechanisms, geometrical

Department of Mechanical Engineering, University of Colorado, 427 UCB, 1111 Engineering Dr, Boulder, CO, 80309, USA.
✉e-mail: francois.barthelat@colorado.edu

hardening, cross-slip, shear-induced dilatancy, and micro-buckling[17–19]. The current report explores, for the first time, the performance and mechanics of these granular crystals subjected to sharp penetration.

Results

Fabrication of granular crystals

We fabricated granular crystals following a protocol that we developed in our previous studies[17,19]. Briefly, millimeter-sized individual grains were first created with a high-resolution light processing 3D printer (EnvisionTEC Micro HiRes), which produced fully dense and isotropic grains with smooth surfaces. The grains were made from an ABS-like photocurable material[20] with a Young's modulus of 3 GPa and a yield strength of 70 MPa. The grains were rhombic dodecahedra (Fig. 1a), a polyhedron that tessellates space to generate fully dense face-centered cubic (FCC) crystalline structures (Fig. 1). Rhombic dodecahedra are an attractive geometry because they are regular polyhedra with high symmetries, which translates into high symmetries in the FCC crystals they form in a close-packed arrangement. In contrast, truncated octahedra that form BCC crystals are not regular, which makes assembly more difficult, leading to BCC crystals that are non-closed packed[17]. Another possible shape is trapezo-rhombic dodecahedra, which has fewer symmetries than rhombic dodecahedra. The HCP crystals formed by this type of grain are close-packed, but they are more anisotropic and more difficult to assemble and characterize[21]. To fabricate FCC crystals from rhombic dodecahedra grains, 1600 grains were gradually poured into a 70 mm × 70 mm × 70 mm acrylic container, which was vibrated vertically (2 mm amplitude and 18 Hz frequency) during the pouring process. Crystallization occurred layer-by-layer, and the assembly process was completed in about 30 min (Fig. 1d).

The first grains poured into the vibrating container rapidly assembled into their lowest energy state, forming a close-packed ⟨111⟩ layer on the flat floor of the container. Additional grains poured into the container naturally formed stacks of ⟨111⟩ layers, until a full "off-axis" crystal was created (Fig. 1b). We also created crystals with an "on-axis" textures with the ⟨110⟩ crystallographic orientation matching the normal to the surface of the crystal (Fig. 1c). This orientation was labeled "on-axis" because when loaded with a vertical load, the forces are channeled along the axis of columns of grains with flat-on-flat contact perpendicular to the columns. The on-axis orientation was more difficult to obtain from a simple container because the first grains deposited must assemble in a non-close-packed layer, which is not possible on a flat floor. To achieve the desired ⟨110⟩ texture, we placed a 3D printed template with a ⟨110⟩ morphology on the floor of the container, before starting the crystallization process. The template successfully induced the proper ⟨110⟩ texture in the first layer of grains, and each layer subsequently added served as a template for the next layer until a full on-axis crystal was created. After crystallization of each layer of grains, we visually checked if the crystallographic alignment of grains was correct and applied longer vibrations if the alignment of grains was not correct. Visual inspection revealed near-perfect crystals, with only a few defects located near the surface and mainly in the form of misrotated individual grains. As a reference, we also fabricated spherical grains of the same material and same volume ($V_g = 132\ mm^3$) as the rhombic dodecahedral grains. The spherical grains were either poured to create randomly packed distributions (RPS, with a measured packing fraction of about 0.59) or crystallized into close-packing spheres using vibrations (CPS with a measured packing fraction of about 0.74).

Penetration tests on granular crystals

After assembly, the single granular crystals and their container were transferred into a standard testing frame (ADMET eXpert 5603) mounted with a 53 mm long cylindrical indenter with a 3 mm radius semi-spherical tip, which was 3D printed using the same printer and material as the grains. The crystal in its container was placed on a platform below the indenter, so that the indenter was roughly centered on its upper surface. The indentation test was performed by slowly driving the indenter (0.33 mm/s) into the surface of the crystal while recording the penetration force. Figure 2a shows results for the penetration tests on randomly packed spheres (RPS) and close-packed spheres (CPS), with three tests for each. The penetration force for RPS rises relatively slowly with penetration distance. Snapshots of the sample taken during the indentation test (Fig. 2c) show that as the indenter is pressed into the random spheres, the spherical grains rotate and displace sideways from the indenter, producing little resistance to penetration and an overall fluid-like response[15]. These results are consistent with previous reports on the penetration of granular medium composed of spheres[5–7,15], with friction of the spheres on the flank of the indenter as the largest contribution to penetration resistance. We attributed the variation of penetration strength for RPS to the randomness of grain distributions.

The penetration force for the close-packed spheres (CPS) was consistently higher than for RPS (we tested three samples for each case), with a maximum penetration force about 2.5 times higher (Fig. 2b). In this study, we also used the term "hardness" in reference to traditional indentation on crystalline materials, but we define it as the maximum penetration during the penetration test. Figure 2d shows snapshots of a CPS sample during the indentation test. As the indenter penetrated the first close-packed layer, it pushed the spheres sideways, causing in-plane compression of the spherical layer, which resulted in a few spheres sliding and rolling upwards out of the layer. Once the first layer was defeated, the same process occurred on the second layer, and then on each of the deeper layers. In some cases, the sudden defeat of a layer was characterized by a small "explosive" failure, with the sphere suddenly ejected out of the surface. This in-plane compression of the layers, together with the reduced mobility of the spheres compared to the RPS samples, explained the higher "hardness" of the CPS samples. The mechanical response of the CPS and RPS samples was governed by frictional sliding and changes in the conformation of the grains. Individual spheres deformed, but only at small strains and within elastic limits. The maximum force of 15 N for the sphere-based sample corresponds to a maximum contact pressure of about 95 MPa (using the radius of the spheres and the

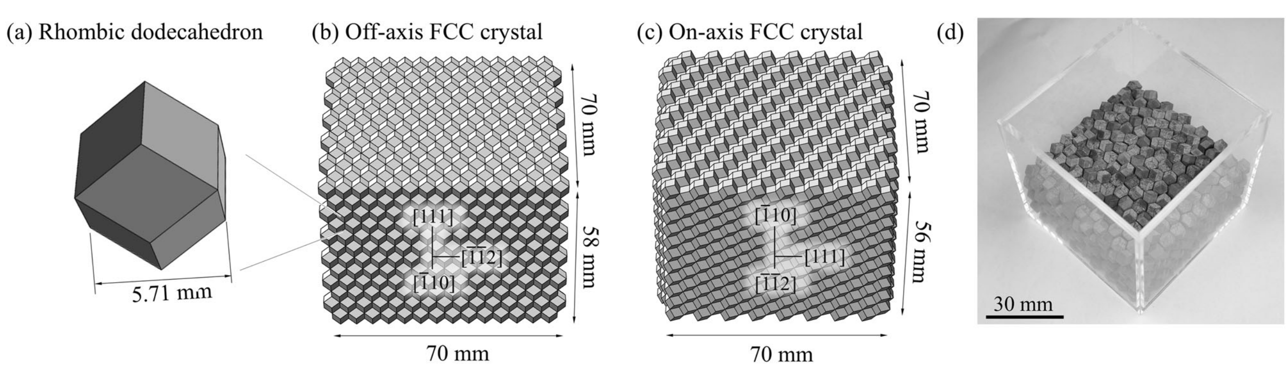

Fig. 1 | FCC granular crystals. **a** Diagram of the individual grain geometry and **b**, **c** FCC granular crystals in two different orientations (off-axis and on-axis); **d** picture of the FCC off-axis crystal.

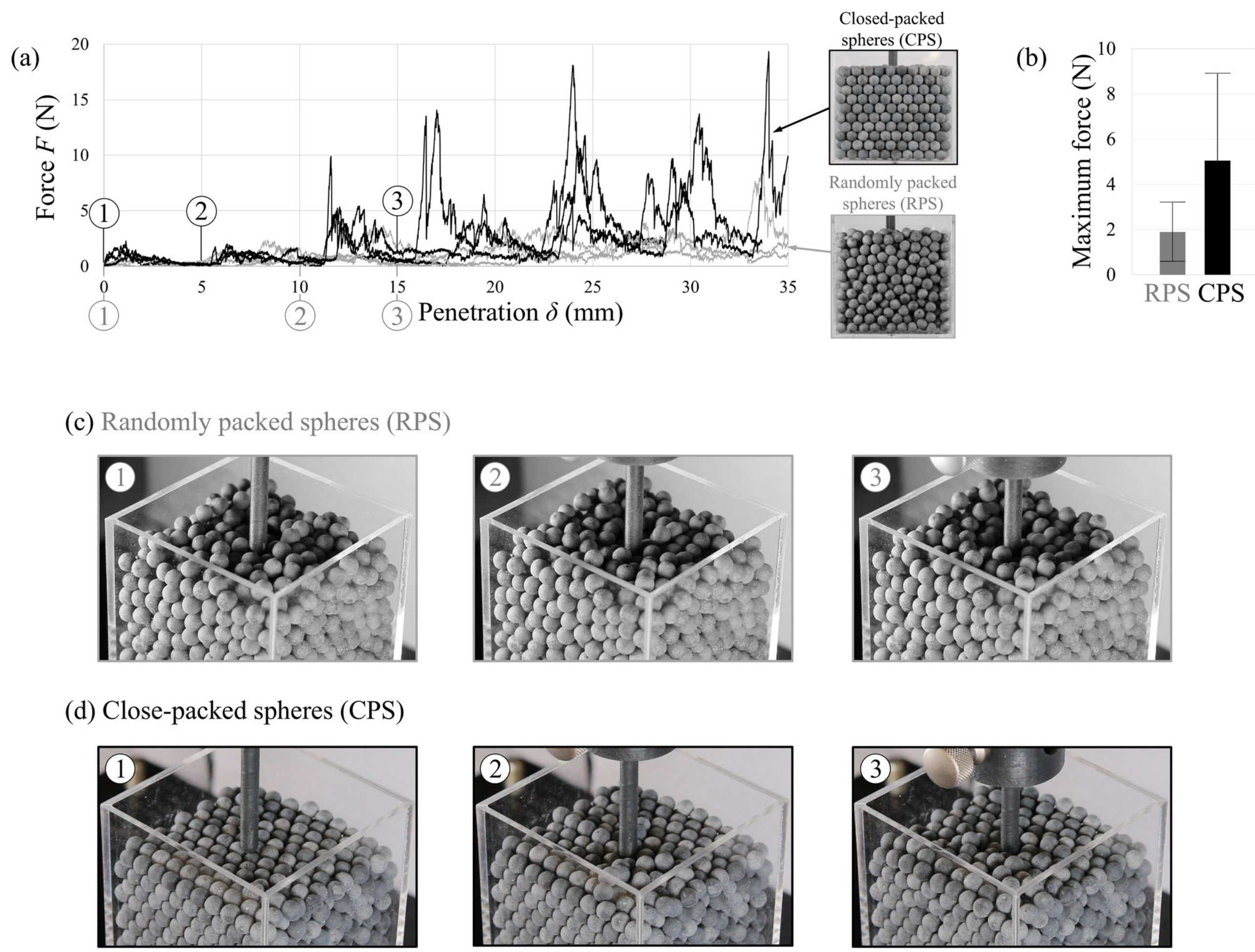

Fig. 2 | Penetration tests results on sphere-based granular beds. **a** Force–penetration curves; **b** maximum forces for random spheres and close-packed spheres (the error bars represent the standard deviation of maximum forces); snapshots of the samples at different stages of penetration: **c** randomly packed spheres (RPS); **d** close-packed spheres (CPS).

elastic properties of the grains[17,22]). The corresponding maximum shear stress[22] is about 30 MPa, which is below the yield shear strength of the material[17] (35 MPa). Indeed, there was no evidence of plastic deformations in the spherical grains, and they could be recycled for other tests with no loss of mechanical performance. The sudden failures of the CPS samples suggest that they are governed by mechanical instabilities, most likely buckling along the horizontal direction. This type of instability is very sensitive to small defects, including small misalignment of the spheres. For these reasons, we attributed the variations of maximum penetration forces in the CPS samples to small variations in the distribution of these defects.

Figure 3 shows the results for penetration tests on the dodecahedron-based FCC off-axis and FCC on-axis crystals (we tested three samples for each design). These materials were much harder than sphere-based granular materials: The maximum forces for the FCC off-axis crystals were about 660 times higher than RPS, and the maximum forces for the FCC on-axis crystals were about 1600 times higher than random spheres (Fig. 3b). The maximum force was calculated for each layer of crystallized grains corresponding to each peak on the force–penetration curve for an experiment. The force–penetration curves for the FCC crystals also revealed a peculiar response: the force increased nonlinearly up to a peak, at which point an "explosive" failure mode occurred where the upper layer of grains suddenly burst as the indenter went through the first layer of grains (Fig. 3c, d). After this first failure event, the force dropped to zero, and then again increased nonlinearly as the indenter went through the second layer of grains, reaching a peak where the next layer of grains exploded again. As the penetration distance increases, this cycle repeats as the indenter defeats each layer in sequence. The sudden nature of this failure suggested that some elastic energy is stored in the crystal, most likely from the insertion of the indenter between the grains of the uppermost layer, inducing in-plane compressive forces. The accumulation of these compressive forces eventually led to the sudden buckling of the upper layer, releasing the stored elastic energy and reducing the indentation force to zero, until the indenter engaged with the next layer of grains. The penetration forces were the highest for the FCC on-axis, which, in a few instances, even led to the failure of the penetrator (Fig. 3b). However, as in the RPS and CPS samples, the deformations of the individual grains in the FCC crystal were small and within elastic limits. The highest recorded indentation force was 1.2 kN, corresponding to a maximum compressive stress of about 40 MPa in the grains (using their effective cross-section), which is below the yield strength of the polymer[17] they are made of (70 MPa). Individual grains could be recovered after the penetration tests and reused to make new crystals with no loss of mechanical performance (as discussed further below). The nonlinear mechanical response of the crystal could therefore be attributed to grain sliding and changes in grain conformations. There were some variations of mechanical response across crystals, which we explained with small variations in the exact stacking of the grains, by a few mis-rotated grains near the surface, and by small variations in the initial positioning of the indenter.

We computed the energy dissipated during penetration by measuring the area under the force–penetration curve (Fig. 4a). The energy absorption capability of the FCC crystals was about 100 times higher than the sphere-based granular materials, supposedly because of enhanced frictional sliding. However, since in-plane buckling of the upper layers is a prominent failure

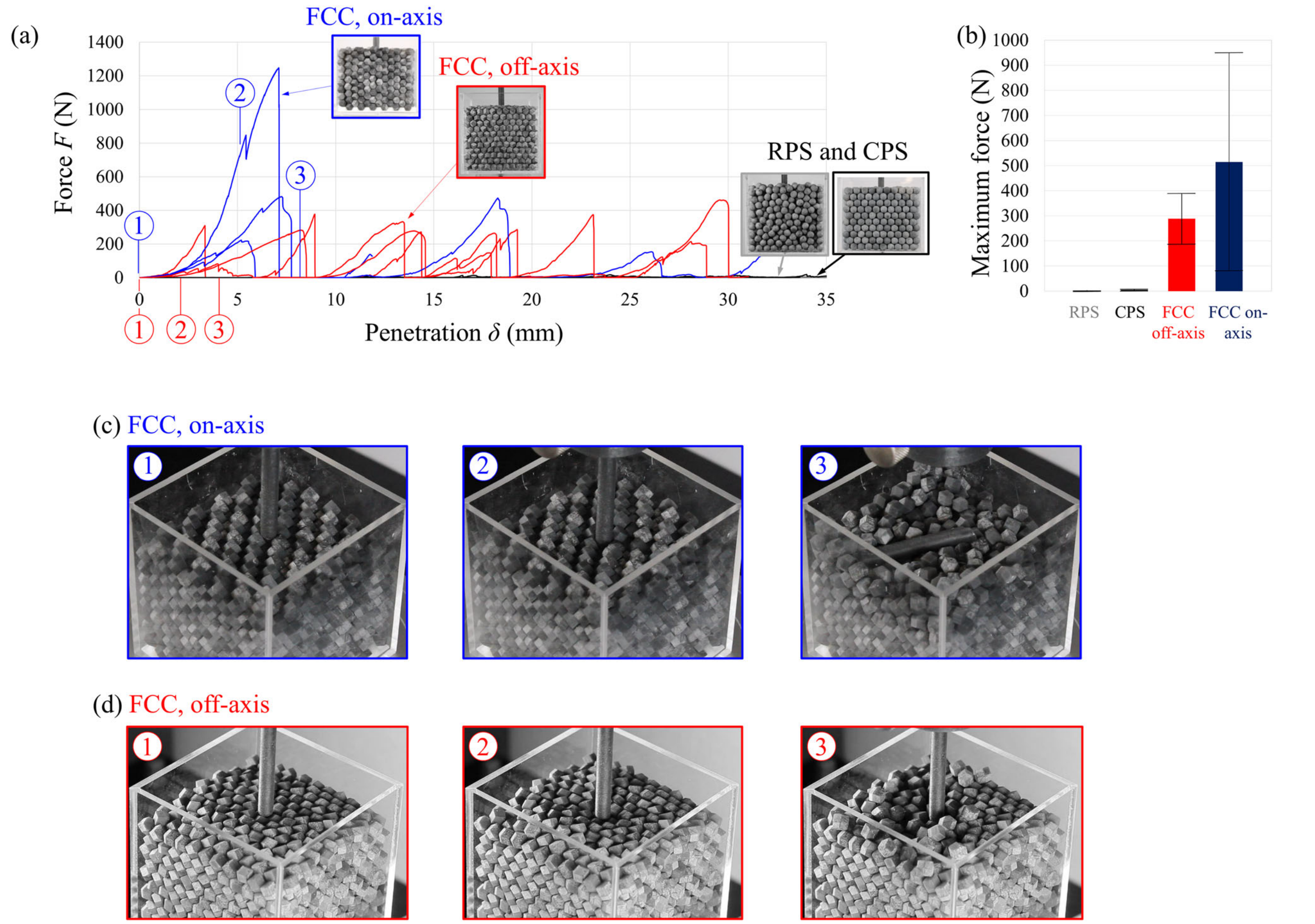

Fig. 3 | Penetration tests results on dodecahedra-based FCC crystals. a Force–penetration curves; **b** maximum forces for FCC off-axis, FCC on-axis and random spheres and close-packed spheres (the error bars represent standard deviations); snapshots of the samples at different stages of penetration: **c** FCC, on-axis and **d** FCC, off-axis.

mechanism in FCC crystals, we also considered the possibility that no sliding or energy dissipative process was actually taking place within the crystal, and that the area under the force–penetration curves could instead reflect elastic energy stored on loading, and then released in the form of kinetic energy in the ejected grains. To elucidate this point, we performed penetration tests on the off-axis crystals, using cyclic loading with gradually increasing amplitudes. A typical result is shown in Fig. 4b: the hysteresis in the curve and the residual penetration displacement clearly indicate that a dissipative process absorbs energy, most likely through non-recovered sliding and shifting of the grains near the penetration area (this type of hysteretic response, in fact, closely resembles typical force–penetration curves from nanoindentation tests on an elastic–plastic metal[23,24]). For each cycle of loading–unloading, we computed the energy dissipated (area of the hysteresis loop) and the elastic energy stored and released upon unloading (area under the unloading curve). The ratio of energy dissipated to energy stored was high for the first cycle (about 8) and gradually decreased to about 1.6 for the fifth cycle. These observations suggest there could be analogies between elastic–plastic nanoindentation and the penetration test on granular crystals, even if the mechanisms at play differ by 6–7 orders of magnitude. As additional evidence for frictional sliding, we performed indentation tests on crystals where the interfaces were lubricated using a food-grade mineral oil. A typical comparison between dry and lubricated crystals is shown in Fig. 4c. Reducing the friction between the grains reduced the apparent indentation stiffness of the crystal as well as the maximum penetration force. Statistical results from the maximum forces and stiffnesses collected from each of the peaks from three experiments on each condition indeed shows a ~50% decrease in apparent indentation stiffness (the slope was measured just prior to explosive failure of the upper layer, Fig. 4d), and a ~30% decrease in maximum indentation force (Fig. 4e). This experiment therefore confirmed that the loading phase of the crystal not only includes elastic deformation, but also inelastic sliding of the grains. Lubricated interfaces lead to easier sliding, which in turn leads to a lower apparent indentation stiffness. Lubrication also decreases the maximum penetration force, suggesting that friction stabilizes the crystal and delays buckling. After a test on a lubricated crystal was completed, the grains were thoroughly cleaned with grease removal soap to recover "dry" grains that could be recycled in new experiments.

Another potential effect we explored experimentally was the size of the granular crystals. These experiments were prompted by size effects in hardness testing and nanoindentation[25,26]. In general, the sample must be sufficiently "large," so its size does not affect the hardness measurements, and so the sample can be interpreted and modeled as a half-space subjected to a localized surface load. To explore the effect of container size L (width of the container) with respect to grain size d, we performed additional indentation tests using five different container sizes. The results (Fig. 5a) show that for smaller containers, the maximum force is higher because of more pronounced mechanical confinement from the walls of the container. As the size of the container is increased, the maximum indentation force decreases, up to about L/d~16, beyond which the maximum force no longer depends on container size.

Finally, we demonstrated the healing capabilities of the granular crystals. We first indented a freshly fabricated FCC crystal until multiple failures occurred (red curve in Fig. 5b). We then recovered the container and the sample, which at that point consisted of an intact lower region and an upper region with randomly distributed grains. The container was then subjected to vibrations of the same amplitude and frequency as those we

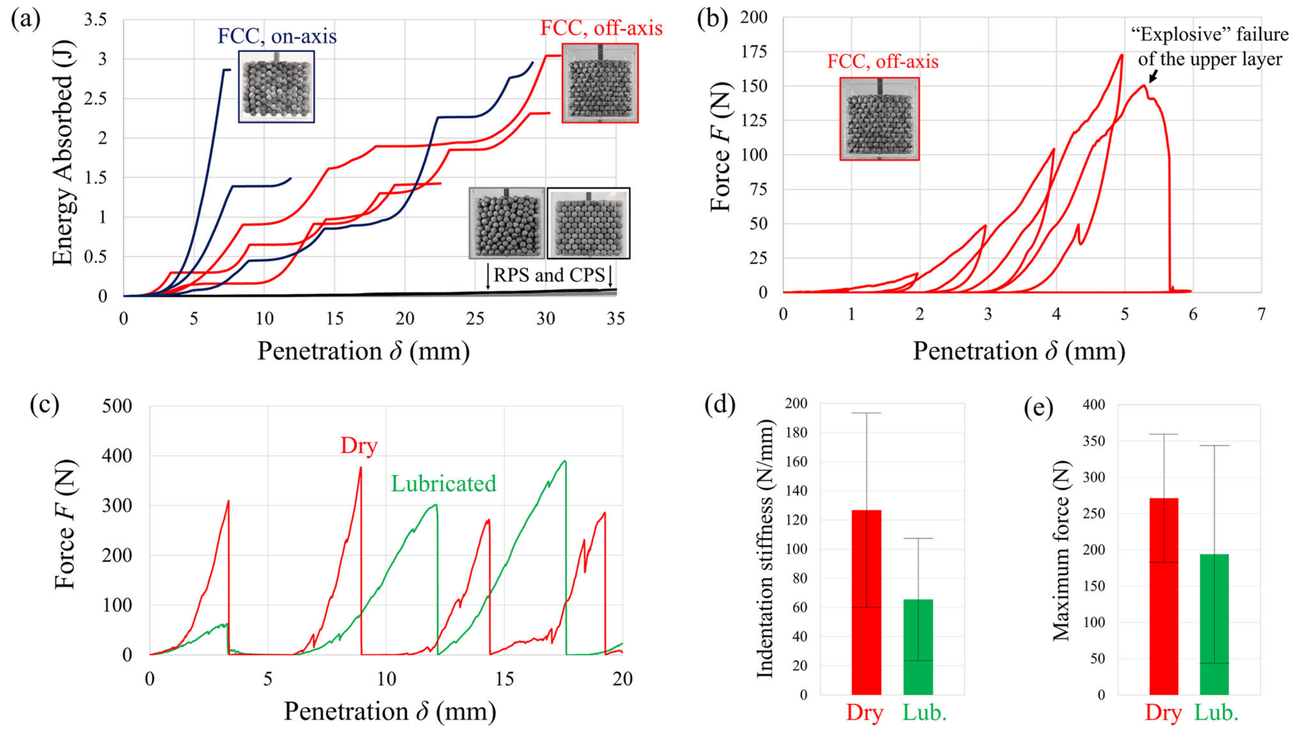

Fig. 4 | Evidence for frictional sliding in FCC crystals. **a** Energy absorption as a function of penetration; **b** force–penetration curve with loading–unloading cycles showing hysteresis; **c** force–penetration curves for dry and lubricated FCC off-axis crystals; **d** stiffness and **e** maximum force for dry and lubricated FCC crystals. The error bars here refer to the standard deviation in all the stiffness and the maximum forces of the dry and lubricated crystals.

Fig. 5 | Additional experiments on FCC crystals. **a** Maximum force as a function of relative container size (L = container size, d = grain size) and **b** force–penetration curve of FCC off-axis crystal after healing.

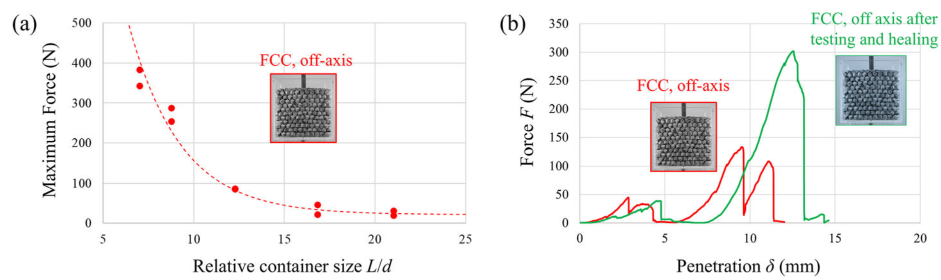

Fig. 6 | DEM model of a granular crystal. **a** A rhombic dodecahedra grain of size d is discretized with overlapping spheres; The rhombic dodecahedra grains are arranged in **b** the FCC off-axis orientation; **c** the FCC on-axis orientation. The crystals are placed inside a container, and the penetration displacement is applied on the indenter at the center of the top layer of grains.

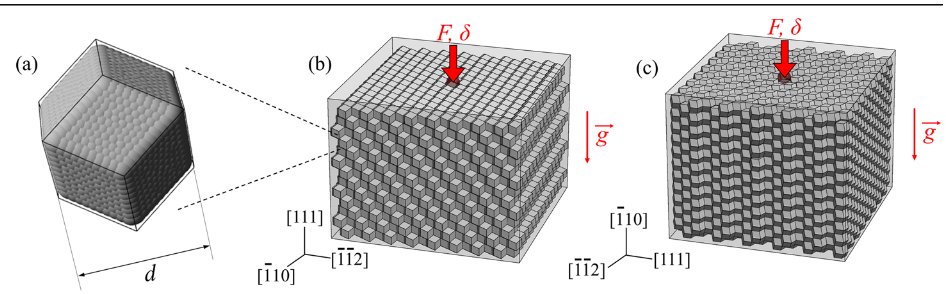

used for assembly. We observed recrystallization, with the damage accrued on the surface of the crystal completely healing. Testing the sample again revealed that there was no loss of strength from this damage-healing cycle (green curve in Fig. 5b). We tested and healed the same sample up to four times with no degradation of mechanical performance, and no apparent degradation in the structure of the grains. The performance of the crystal will probably eventually degrade because of wear of the grains, but it may take many more cycles of testing—healing before any noticeable degradation is noticed.

DEM models on granular crystals

Our previous studies on uniaxial compression on FCC granular crystals showed that {111} slip planes get activated during compression of off-axis samples, while micro-buckling was the prominent mechanism for on-axis samples[17–19]. The indentation experiments presented here show evidence of frictional sliding between the grains and sudden failure, possibly due to buckling from in-plane compressive stresses. In order to capture these mechanisms in detail, we have developed discrete element models (DEM) of the penetration tests. DEM is an ideal method for this granular system, and for this work, we used the granular package in LAMMPS[27]. To capture the dodecahedral shape of the grains, we discretized each of the grains with spheres (Fig. 6a)[18,28,29]. Spheres from the same grains did not interact, and spheres from adjacent grains interacted following simple linear Hooke's law for the contact. An important feature of the sliding of flat surfaces of finite dimensions (facets of the grains) is that the contact force depends not only on the interpenetration distance, but also on the contact area between the facets (which decreases with sliding as the grains progressively lose contact[30]). When the faces of the flat contacts are discretized with spheres, this effect is properly captured because the number of spheres in contact directly reflects the contact area between the grains. This modeling approach, therefore, properly captures the reduced contact forces that come with sliding[18], as opposed to other approaches based on collision between polyhedral grains, where the contact forces depend on interpenetration distance only[31–33]. In this discretized approach, 3076 of these dodecahedral grains were then placed on an FCC lattice, either in the off-axis (Fig. 6b) or on-axis orientation (Fig. 6c). In addition, the crystal was confined by a floor and side walls and subjected to gravity. The penetration force was applied through a sphere with the same diameter as the tip of the indenter used in the experiments. Our experimental observation showed that penetration is resisted by intact layers of grain below the penetrator. Once the grains from the upper layers are defeated, they interact little with the sides of the penetrator, and therefore, modeling the indenter as a sphere captured the essence of the test. At larger penetration depths, the frictional forces of the defeated grain would probably contribute more to penetration resistance, as seen in deep penetration tests on granular beds[14]. However, the penetration depths we used in our tests were too small to reach that regime. We used a friction coefficient of 0.35 (measured experimentally[18]) to capture grain-on-grain frictional contacts.

Preliminary simulations for the penetration tests revealed that the indentation force scales linearly with the elastic modulus E of the grains. We therefore used a stiffness scaling approach to ensure numerical stability of the simulations, and we normalized the forces by Ed^2 (where d = size of the grains). Stiffness scaling is often used in the DEM modeling of granular media composed of stiff grains. In this procedure, the numerical contact stiffness between the grains is reduced compared to the actual contact stiffness to enable longer time steps and to keep computational costs manageable[34–37]. All forces from our DEM models were normalized using the modulus used in the simulations (we checked that these forces linearly scale with modulus). Another important numerical consideration was the discretization of the grains with spheres, which can be captured by two parameters: The number of spheres on the edges of the dodecahedral grain N_e, and the overlap between the spheres κ ($\kappa = 0$: no overlap between spheres and $\kappa = 1$: full overlap). Geometrically, we required that the surface of the spheres was flush (tangent) to the faces of the ideal polyhedra, so that the diameter of the individual spheres was calculated from Ne and κ. Figure 7a shows a set of indentation curves for different combinations of these parameters. We found that $N_e = 5$ and $\kappa = 0.75$ provided a good compromise between accuracy and computational speed, and further refinement of the discretization did not lead to significant changes in the force–penetration curves. In addition, parameters N_e and κ govern the "sharpness" of the edges of the polyhedral grains. With the converged values for these parameters, further refinements led to sharper edges, but these had little effect on the results. The interactions between the grains are therefore dominated by face-on-face frictional contact, the sharpness of the edges having a minimal effect on the results. Figure 7b shows that the predicted force–penetration (F–δ) curves agree well with the experimental trends. The model duplicated the overall shape of the curves, with gradual stiffening until a peak force, then a sharp decrease until another cycle starts. The nonlinear loading and the "explosive" failure of the upper layer were captured, along both on-axis and off-axis loading directions (Fig. 7c-d). There are, however, discrepancies in values between the DEM model and the experiments, which we attributed to the sphere discretization approach to imperfection in the experiments (imperfect contact between grains, point defects, slight variations on the initial positioning of the penetrator).

We used these DEM models to further explore the effects of friction, frictional sliding mechanisms and failure mechanisms. Figure 8 shows the normalized maximum penetration force on an FCC off-axis crystal as a function of the coefficient of friction μ. Higher friction translates to higher penetration resistance, which confirms that frictional sliding plays a major role in the penetration mechanism and strength. With zero friction, the crystal still produced a resistance to penetration, which we attributed to the mechanical confinement of the grains.

Local strains were computed from the relative displacements of the individual grains. We then computed the (Von Mises) equivalent strain, a scalar quantity function of the individual strain components. Figure 9 shows the distribution of the equivalent strains on cross sections of the FCC off-axis and on-axis crystals, just prior to the unstable failure of the upper layer (the initial, stress-free crystal was taken as a reference for the calculation of strains). These plots reveal significant elastoplastic activity in the granular crystal: In the off-axis configuration, the region of maximum equivalent strain is slightly below the surface and under the indenter (Fig. 9a), in consistence with the elastic–plastic indentation stress solution for continuous materials[22,38]. In the on-axis crystal, the deformations are concentrated in columns under the indenter, and in an umbrella-like structure near the surface (Fig. 9b).

Further analysis involved the tracking of the sliding and normal penetration of each interface of the grains within the crystals, which we computed from the relative displacement and rotation of neighboring grains. Plotting these interfaces using a threshold was a useful way to reveal the interfaces that undergo the most sliding and interpenetration. Figure 10a shows the interfaces that undergo the most sliding during the first loading ramp on an FCC crystal in the off-axis loading orientation. A clear pattern emerged: three {111} slip planes get activated in the bulk of the crystal to form a pyramidal structure with the apex at the indenter, which provides additional evidence that frictional sliding occurs deep in the bulk of the crystal. By tracking the amount of normal interpenetration between the faces of neighboring grains, we highlighted the interfaces that are the most compressed within the crystal (Fig. 10b). As expected, a volumetric region of high compressive forces (with a roughly pyramidal shape) develops underneath the indenter. In addition, the results show a significant amount of compression developing in the uppermost layer of grains and in plane (highlighted in red). Interestingly, these surface regions are mostly concentrated within two lines, matching the shortest distances from the indenter to the wall of the container. Evidently, as the indenter is wedged between the grains in the center of the crystal, the surface grains are displaced in-plane, and some of these grains become abutted by the container walls. This in-plane compression is finally responsible for the sudden buckling and "explosive" failure of the upper layer.

The FCC on-axis crystal developed other sets of deformation mechanisms. The visualization of sliding interfaces (Fig. 10c) revealed the formation of two {112} slip planes (highlighted in blue), an unusual phenomenon in FCC crystals. Our previous work on uniaxial deformation showed that along the on-axis direction, inelastic deformation by {111} slip was completely forbidden[17,19]. In these previous experiments, buckling then became the prominent failure mechanism. In the indentation experiments, the lateral confinement of the crystal prevents the buckling of the central column of grains, and instead, it is an unusual set of {112} slip planes that get activated. In addition, we observed some sliding on a cylindrical region centered on the indentation site (highlighted in red on Fig. 10c). Finally, Fig. 10d shows that the interfaces subjected to a large compressive force are concentrated along a cross-like structure that spans the entire depth of the sample. The central columns of grains are confined laterally by the rest of the crystal, so that the buckling of the crystal is prevented by these surrounding grains. This mechanism is the likely cause of these compressive regions between the central region of the crystal and the container walls.

Discussion

The sharp penetration of granular materials is a highly relevant problem for a variety of applications, including the locomotion of animals and robots on

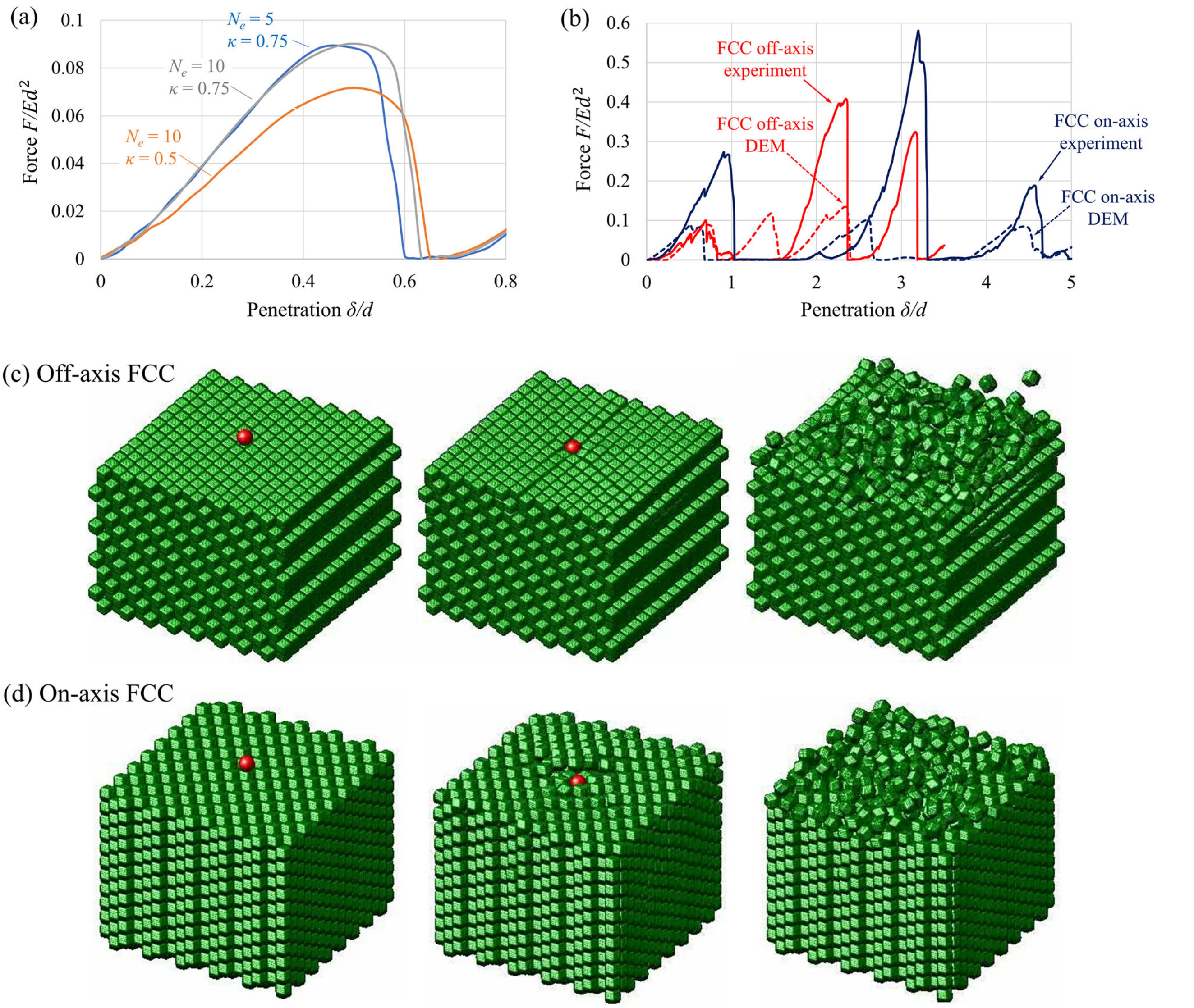

Fig. 7 | DEM results on granular crystals. a Normalized force–penetration curves for FCC off-axis crystals using different parameters for sphere discretization; **b** normalized force–penetration curves for FCC off-axis and FCC on-axis crystals from DEM models (shown in dotted lines) and from experiments (shown in solid lines); snapshots of the models at different stages of penetration for **c** off-axis and **d** on-axis FCC crystals.

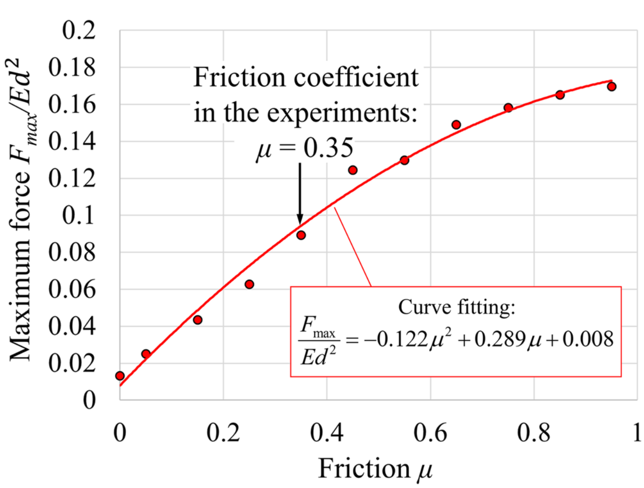

Fig. 8 | Effect of friction coefficient on the maximum penetration force. The value of the friction coefficient in the experiments is shown. The data was fitted with a polynomial function to highlight the non-linear increase of the maximum force with the friction coefficient.

sandy grounds, defensive structures or civil constructions. In traditional granular materials, the grains "flow" around the advancing penetrator like a viscous liquid, which involves frictional dissipation, with limited resistance to penetration. In this report, we have characterized the mechanical performance and mechanics of fully dense FCC granular crystals subjected to sharp penetration. We found that these crystals are about 1000 times more resistant to penetration than traditional granular materials made of randomly distributed spheres, and that they can dissipate about 100 times more penetration energy. Further, we characterized the mechanisms of deformation and failure in these granular crystals using imaging and discrete element models. Despite the high mechanical confinement of the crystals we found that frictional sliding is a prominent deformation mechanism up to the failure of the uppermost layer of grains, and that this sliding occurs along specific slip planes which depend on the orientation of the crystal: {111} slip planes for the "off-axis" orientation and, unexpectedly for a FCC crystal, {112} slip planes for the "on-axis" orientation. Meanwhile, as the indenter is "wedged" between the grains, large compressive forces develop in the transverse directions, which eventually lead to the sudden buckling of the uppermost layer of grains and "explosive" failures involving the ejection of grains. As penetration proceeds, this loading-buckling cycle repeats, as

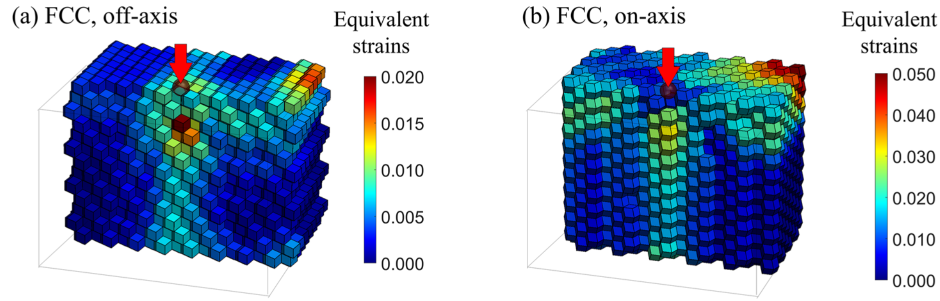

Fig. 9 | Deformation patterns in granular crystals. Equivalent strains on a cross section of **a** the FCC, off-axis crystal; **b** the FCC, on-axis crystal.

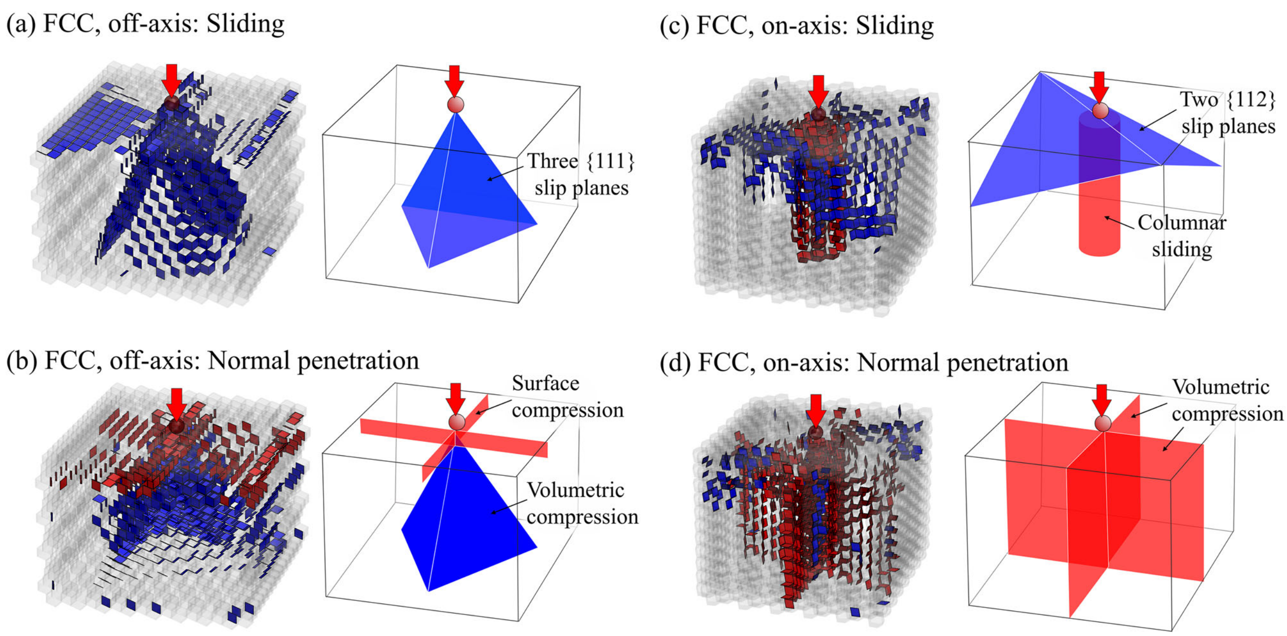

Fig. 10 | Force transfer in granular crystals prior to first failure. Prominent sliding interfaces and compressive interfaces (normal penetration) for **a**, **b** FCC off-axis crystal and **c**, **d** FCC on-axis crystal. For **a**, **c**, only the interface where sliding >0.004 *d* (off-axis) and sliding >0.017 *d* (on-axis) are colored, according to the deformation structure (blue = slip planes, red = columnar sliding). For **b**, **d**, only the interface where penetration >0.0012 *d* (off-axis) and penetration >0.0015 *d* (on-axis) are colored, according to the deformation structure.

layers are defeated in sequence. As expected, the penetration resistance increases when the grains are placed in smaller containers, which provide more mechanical confinement. On the other hand, we showed that if the container is sufficiently large (side length about 16 times the size of grains), a converged response independent of container size is achieved. Our results show that the resistance to penetration of these macroscale crystals is governed by elastic deformation and frictional sliding, which are not size-dependent mechanisms. These granular crystals could be scaled up with the same deformation mechanisms and nondimensional performance (i.e., same forces F/Ed^2). The granular systems could also be scaled down with the same results, as long as the physics of interaction remain unchanged. Below some size, a "colloidal" regime would probably prevail, with stronger surface forces between the grains. A major benefit of the granular crystals is that they can be easily assembled and disassembled using mild mechanical forces, like the mechanical vibrations we have used in this report. We also showed here that once the surface layers of the crystal are destroyed by the penetrator, the crystal can be "healed" with vibrations and then punctured again with no loss of mechanical performance. These perfect granular "metamaterials" can serve as a platform to develop additional design strategies, for example, by manipulating the interfaces between the grains (increasing friction, or using adhesives[19]), or by manipulating the geometry of the grains[21]. Further, since the inelastic deformation mechanisms by slip planes are similar to traditional plasticity at the atomic scale, strengthening strategies inspired by metallurgy may be implemented in the future, for example, solid solution strengthening or grain boundaries. We envision that these enhanced granular "metamaterials" will find applications for rapid and versatile construction of static structures or as lightweight protective materials in a multitude of applications (e.g., buildings, body armor, and vehicles).

Data availability

All data are available in the main text or the Supplementary Information.

Received: 31 October 2025; Accepted: 30 January 2026;
Published online: 13 March 2026

References

1. Behringer, R. P. & Chakraborty, B. The physics of jamming for granular materials: a review. *Rep. Prog. Phys.* **82**, 012601 (2018).
2. Radjai, F., Roux, J.-N. & Daouadji, A. Modeling granular materials: century-long research across scales. *J. Eng. Mech.* **143**, 04017002 (2017).
3. Behringer, R. P. et al. Statistical properties of granular materials near jamming. *J. Stat. Mech. Theory Exp.* **2014**, P06004 (2014).
4. Roth, L. K. Constant speed penetration into granular materials: drag forces from the quasistatic to inertial regime. *Granul. Matter* **23**, 54 (2021).
5. Liang, S., Liu, L. & Ji, S. DEM simulations of resistance of particle to intruders during quasistatic penetrations. *Comput. Model. Eng. Sci.* **128**, 145–160 (2021).

6. Hamm, E., Tapia, F. & Melo, F. Dynamics of shear bands in a dense granular material forced by a slowly moving rigid body. *Phys. Rev. E* **84**, 041304 (2011).
7. Paume, V., Aussillous, P. & Pouliquen, O. Finite size effects during the penetration of objects in a granular medium. https://doi.org/10.1039/D3SM01242E (2023).
8. Pirrone, S. R. M., Del Dottore, E. & Mazzolai, B. Historical evolution and new trends for soil-intruder interaction modeling. *Bioinspir. Biomim.* **18**, 011001 (2022).
9. Roth, L. K., Han, E. & Jaeger, H. M. Intrusion into granular media beyond the quasistatic regime. *Phys. Rev. Lett.* **126**, 218001 (2021).
10. Hou, M. et al. Projectile impact and penetration in loose granular bed. *Sci. Technol. Adv. Mater.* **6**, 855 (2005).
11. Tapia, F., Espíndola, D., Hamm, E. & Melo, F. Effect of packing fraction on shear band formation in a granular material forced by a penetrometer. *Phys. Rev. E* **87**, 014201 (2013).
12. Katsuragi, H. & Durian, D. J. Unified force law for granular impact cratering. *Nat. Phys.* **3**, 420–423 (2007).
13. Clark, A. H. & Behringer, R. P. Granular impact model as an energy-depth relation. *Europhys. Lett.* **101**, 64001 (2013).
14. Askari, H. & Kamrin, K. Intrusion rheology in grains and other flowable materials. *Nat. Mater.* **15**, 1274–1279 (2016).
15. Kang, W., Feng, Y., Liu, C. & Blumenfeld, R. Archimedes' law explains penetration of solids into granular media. *Nat. Commun.* **9**, 1101 (2018).
16. Athanassiadis, A. G. et al. Particle shape effects on the stress response of granular packings. *Soft Matter* **10**, 48–59 (2014).
17. Karuriya, A. N. & Barthelat, F. Granular crystals as strong and fully dense architectured materials. *Proc. Natl. Acad. Sci. USA* **120**, e2215508120 (2023).
18. Karuriya, A. N. & Barthelat, F. Plastic deformations and strain hardening in fully dense granular crystals. *J. Mech. Phys. Solids* **186**, 105597 (2024).
19. Karuriya, A. N., Simoes, J. & Barthelat, F. Fully dense and cohesive FCC granular crystals. *Extrem. Mech. Lett.* **71**, 102208 (2024).
20. E-Rigid Form. *ETEC* https://envisiontec.com/material/e-rigid-form/.
21. Gao, T., Karuriya, A. N. & Barthelat, F. Comparing inelastic deformations and strength in dense FCC and HCP granular crystals: Experiments and models. *J. Mech. Phys. Solids* **204**, 106305 (2025).
22. Johnson, K. L. *Contact Mechanics*. (Cambridge University Press, Cambridge, 1985). https://doi.org/10.1017/CBO9781139171731.
23. Zhang, D. & Li, D. Y. A further look at the nano/micro-indentation method for measuring and ranking Young's modulus and hardness of materials. *Phys. Scr.* **98**, 095936 (2023).
24. VanLandingham, M. R., Villarrubia, J. S., Guthrie, W. F. & Meyers, G. F. Nanoindentation of polymers: an overview. *Macromol. Symp.* **167**, 15–44 (2001).
25. Fleck, N. A., Muller, G. M., Ashby, M. F. & Hutchinson, J. W. Strain gradient plasticity: theory and experiment. *Acta Metall. Mater.* **42**, 475–487 (1994).
26. Pharr, G. M., Herbert, E. G. & Gao, Y. The indentation size effect: a critical examination of experimental observations and mechanistic interpretations. *Annu. Rev. Mater. Res.* **40**, 271–292 (2010).
27. Thompson, A. P. et al. LAMMPS—a flexible simulation tool for particle-based materials modeling at the atomic, meso, and continuum scales. *Comput. Phys. Commun.* **271**, 108171 (2022).
28. Kruggel-Emden, H., Rickelt, S., Wirtz, S. & Scherer, V. A study on the validity of the multi-sphere discrete element method. *Powder Technol.* **188**, 153–165 (2008).
29. Garcia, X., Latham, J.-P., Xiang, J. & Harrison, J. P. A clustered overlapping sphere algorithm to represent real particles in discrete element modelling. *Géotechnique* **59**, 779–784 (2009).
30. Dalaq, A. S. & Barthelat, F. Strength and stability in architectured spine-like segmented structures. *Int. J. Solids Struct.* **171**, 146–157 (2019).
31. Bahmani, A., Pro, J. W., Hannard, F. & Barthelat, F. Vibration-driven fabrication of dense architectured panels. *Matter* **5**, 899–910 (2022).
32. Mittal, A., Mangadoddy, N. & Banerjee, R. GPU based discrete element modeling for convex polyhedral shape particles: development and validation. *Powder Technol.* **449**, 120407 (2025).
33. Keissar, Y., Gardner, M. & Sitar, N. A new algorithm for accurate contact point calculation between convex polyhedral particles in DEM. *Comput. Geotech.* **184**, 107240 (2025).
34. Zhang, Y., Li, L., Zhang, Y. & Li, L. Optimization of discrete element method model to obtain stable and reliable numerical results of mechanical response of granular materials. *Minerals* **14**, 8 (2024).
35. Washino, K., Chan, E. L. & Tanaka, T. DEM with attraction forces using reduced particle stiffness. *Powder Technol.* **325**, 202–208 (2018).
36. Kellogg, K. M. et al. Discrete-Element-Method-Based Determination of Particle-Level Inputs for the Continuum Theory of Flows with Moderately Cohesive Particles. *Processes* **11**, 2553 (2023).
37. Radjai, F. & Dubois, F. *Discrete-Element Modeling of Granular Materials*. (Wiley-Iste, 2011).
38. Brian, L. Fracture of Brittle Solids. 194 https://doi.org/10.1017/cbo9780511623127 (1993).

Acknowledgments
This work was sponsored by the Army Research Office under Grant Number: W911NF-24-2-0126. The views and conclusions contained in this document are those of the authors and should not be interpreted as representing the official policies, either expressed or implied, of ARO or the U.S. Government. The U.S. Government is authorized to reproduce and distribute reprints for Government purposes, notwithstanding any copyright notation herein.

Author contributions
F.B. conceived the idea. A.N.K. performed the experiments. A.N.K. and F.B. conducted simulations. A.N.K. and F.B. analyzed and interpreted the results. A.N.K. and F.B. wrote the paper. F.B. contributed to both funding acquisition and project management.

Competing interests
The authors declare no competing interests.

Additional information
Correspondence and requests for materials should be addressed to Francois Barthelat.